Numerical analysis of turbulence characteristics in a flat-plate flow with riblets control

Yang Zhang, Zhixian Ye, Binghua Li, Lan Xie, Jianfeng Zou[*] and Yao Zheng

*Correspondence:
zoujianfeng@zju.edu.cn

Center for Engineering
and Scientific Computation,
School of Aeronautics
and Astronautics, Zhejiang
University, Hangzhou 310027,
China

Abstract

A comparative study about riblets-controlled turbulent boundary layers has been performed to investigate the turbulence characteristics associated with drag reduction in a compressive flat-plate flow (where the free-stream Mach number is 0.7) by means of direct numerical simulations (DNSs). With a setting of the triangular riblets ($s^+ \approx 30.82$, $h^+ \approx 15.41$) settled on the $Re_\tau \approx 500$ turbulent boundary layer, an effective global drag reduction was achieved. By comparing velocity and its fluctuation distribution, vorticity fluctuation and streaks structures between the smooth and riblets flat-plate cases, two roles of lifting and rectification in terms of riblets drag control are revealed that the micro-scale riblets can lift up logarithmic-law region of the boundary layer, which leads to a smaller wall friction velocity and thus a drag reduction. The streamwise vortices and its fluctuation structures are shifted upward, thus the interactions between them and the wall surface are weakened, which causes the suppressed intensity of Reynolds normal stresses, streamwise vorticity and turbulent kinetic energy production inside the riblets. Moreover, the streaks associated with streamwise velocity or 3D vortices are ruled from the distorted to long and straight structures as they pass through the riblets, indicating an ability of riblets to turn turbulence into a more ordered state.

Keywords: Riblets control, Drag reduction, Turbulent boundary layer, Large-scale simulation

1 Introduction

The design of the riblets control strategy is inspired by the surface structure of sharkskin in nature. Scientists found that there are many rough ridged structures on the shark's skin, which can effectively reduce the shark's drag to flow in fast swimming [1, 2]. This discovery breaks the traditional concept that the smoother the surface of an object, the lower the drag during flow. As a passive control technique, riblets control requires neither supplementary actuators nor manual input of system energy, thus attracting much attention from researchers. Luchini, Manzo, Pozzi [3] and Bechert, Bruse, Hage, et al. [4] investigated the effect of different riblets structures and sizes on the performance of riblets drag reduction. They found that sawtooth riblets and semi-circular scalloped riblets can obtain the best drag reduction ratio when the lateral rib spacing width $s^+ \approx 15$,

and an improved 8.7% skin-friction reduction can be acquired for an adjustable surface with longitudinal blade ribs. García-Mayoral & Jiménez [5–7] considered that the riblets cross section A_g^+ may be a better characteristic parameter than the riblets spacing, with an optimum $A_g^+ = 10.7$. Considering the three-dimensional shape features of the real sharkskin, Sasamori, Mamori, Iwamoto, et al. [8] experimentally studied the three-dimensional sinusoidal riblets flow control in a fully developed turbulent channel flow at a low turbulent Reynolds number $Re_\tau \approx 150$. The lateral spacing of the adjacent walls of the riblets varied sinusoidally in the streamwise direction. They found that the drag reduction mechanism is similar to that of two-dimensional streamwise riblets. The difference is that its wetted area is smaller than the two-dimensional riblets, thus obtaining a higher drag reduction performance.

Due to the complexity of turbulence itself and the limitations of experimental measurement techniques, there are still different views on the understanding of the flow mechanism of riblets-controlled drag reduction. One view is that riblets act as a lift-up effect to the boundary layer [9, 10]. The flow inside the riblets is blocked by viscosity, making the viscous bottom layer thicker, which reduces the fluid velocity gradient near the wall while weakens the interaction between the streamwise vortex and the wall. Lee & Lee [11] used particle image velocimetry and a high-speed camera and captured that the flow vortices near the wall were concentrated at the tip of the riblets and that the flow near the valley area was smooth, further supporting this idea. Another view is that the riblet tips influence the streamwise vortices at the viscous sub-layer and a couple of regenerated secondary vortices form on both sides of the riblet tip [12]. These secondary vortices make the strength of the streamwise vortice weaker, suppressing the lifting, oscillation and breaking up of the low-speed streaks. Martin & Bhushan [13, 14] and Bhushan & Dean [15, 16] supported the first drag-reduction mechanism by analyzing continuous and segmented riblets structures and flow properties. They explored the relationships among the vortices, riblets geometry and drag-reduction rate as well. The optimal drag reduction was obtained, as the vortices were about 1.5 times as large as the riblets spacing. The corresponding riblets spacing was $s^+ \approx 18 \sim 25$, which was on the same order with $s^+ \approx 16 \sim 18$ by Bechert, Bruse, Hage, et al. [4] and El-Samni, Chun & Yoon [17].

Considering the large amount of simulation due to the micro-flow near riblets, most numerical calculations were thus far performed in low Reynolds number channel flow. Choi, Moin & Kim [18] performed a direct numerical simulation of a fully developed turbulent channel flow over a two-dimensional (2D) riblets surface. The bulk Reynolds number Re_b with the channel half-width was 4200 and the turbulent Reynolds number Re_τ was about 180. They reported that the riblets affected streamwise vortices in the near-wall region, because the lateral spacing of the riblets was smaller than the size of streamwise vortices. The numerical study of the laminar and low turbulent Reynolds number channel flow by Chu & Karniadakis [19] suggested that there was no drag reduction in the laminar regime for the riblets wall in comparison with the smooth wall of the channel, whereas approximately 6% drag reduction existed in low turbulent regimes with $Re_b = 3500$. The three-dimensional dentils on the real shark skin were replicated by Boomsma & Sotiropoulos [20] and were numerically simulated in a channel flow at $Re_\tau = 180$. They found that the three-dimensional geometry of the shark skin generates

strong secondary flow within the boundary layer, strengthens turbulent mix and promotes Reynolds stress, thus increasing the wall friction. However, the sinusoidal riblets will induce stable counter-rotating vortices on both sides of the riblets tips and are able to block strong shear stresses above the tips, thus providing a drag reduction effect. This is consistent with the results from the experimental evidence of Bechert, Bruse & Hage [10]. However, this is contrary to the conclusions by Wen, Weaver & Lauder [21], possibly due to differences in flow conditions. Most importantly, it is difficult to obtain the realistic shear stress distribution of shark skin, and thus it is difficult to understand the reason why the three-dimensional dentils surface of the imitation shark skin increases drag while the riblets structure decreases drag at correct size.

Unlike the channel flow, in the present study, large-scale simulations on flat-plate turbulent boundary layers in a medium Reynolds number have been carried out in both riblets and smooth cases. In fact, the industrial application of riblets control in aircraft flight is very promising and will bring great economic benefits [22–24], thus the spatial developing turbulent flow on the aircraft surface is closer to reality. Riblets used in internal flows, because of the mass flow constraint, may behave quite differently than in external flows, though the similar drag-reduction performance with 3 M riblets in fully developed pipe and developing flat plate flows, reported by Rohr, Andersen, Reidy, et al. [25]. However, in their study the turbulent features were not compared in detail as a result of the differences of internal and external flows. Klumpp, Meinke & Schröder [26] investigated the effect of riblets on the three-dimensional transition on a zero-pressure-gradient developing turbulent boundary layer at $Re_\tau < 250$ by LES. They found that the 2D Tollmien-Schlichting (T-S) waves were amplified by riblets, whereas 3D hairpin and streamwise vortices were damped. Boomsma & Sotiropoulos [27] compared drag reduction by scalloped riblets in a zero pressure gradient and mild Adverse Pressure Gradients (APG) boundary layers using high-resolution large eddy simulations. The results showed that there was only a slight improvement in drag reduction for riblets in the mild APG. The lift-drag characteristics were discussed by Zhang, Chen, Fu, et al. [28, 29] in a low-speed airfoil flow using riblets control. The effects of converging–diverging riblet-type surface roughness on the boundary layer were investigated in a flat plate flow [30]. The results reported that the directional surface roughness pattern induced a large-scale spanwise periodicity onto the boundary layer, thus it modified the boundary layer thickness. It is noticeable that in their experiments the turbulent Reynolds number $Re_\tau = 771 \sim 3000$ is large enough, since the numerical calculation at the same level of Reynolds number flow is very expensive.

The objective of the present study is to numerically examine the drag-reduction effect of the 2D riblets and to reveal the evolution of turbulent structures by comparing the riblets flat flow and the smooth flat flow at a medium Reynolds number, which is helpful to the understanding of the riblets flow mechanism. In order to approach the actual flight conditions as much as possible, a subsonic compressive turbulent flat plate flow at $Ma_\infty = 0.7$ will be resolved with a high-order finite difference DNS solver. The turbulent transition is enforced by means of the unsteady blowing/suction disturbance near the inlet. The length of the flat plate is long enough with 30 inch and the 2D triangle riblets are installed in the rear position of the smooth flat plate. The turbulent Reynolds number Re_τ can reach approximate 500 in the downstream corresponding

to the momentum Reynolds number $Re_\theta \approx 2320$. The results of the average velocity profile at different locations of riblets, drag reduction, turbulent fluctuation and three components of vorticity fluctuation are evaluated. The differences generated by riblets are revealed to illustrate the roles of riblets control in a flat-plate turbulent boundary layer.

2 Computation model

2.1 Control equations of Newtonian fluid

The law of Newtonian fluid motion can be characterized by Navier–Stokes (N-S) equations, including mass equation, momentum equation and energy conservation equation, as follows,

$$\frac{\partial \rho}{\partial t} + \frac{\partial \rho u_j}{\partial x_j} = 0, \tag{1}$$

$$\frac{\partial \rho u_i}{\partial t} + \frac{\partial \rho u_i u_j}{\partial x_j} = -\frac{\partial p}{\partial x_i} + \frac{\partial \tau_{ij}}{\partial x_j}, \tag{2}$$

$$\frac{\partial \rho E}{\partial t} + \frac{\partial (\rho E + p) u_i}{\partial x_i} = -\frac{\partial q_i}{\partial x_i} + \frac{\partial u_i \tau_{ij}}{\partial x_j}, \tag{3}$$

which are non-dimensioned by the corresponding free inflow parameters. The dimensionless density, velocity, pressure and energy are $\rho = \rho^*/\rho_\infty^*$, $u = u^*/u_\infty^*$, and $p = p^*/(\rho_\infty^* u_\infty^{*2})$, and $E = E^*/u_\infty^{*2}$, respectively. In the current numerical model, the characteristic length L_∞ is set to be 1 inch, so the non-dimensioned time is $t = t^* \times u_\infty^*/L_\infty$, where the subscript ∞ denotes free inflow and the superscript $*$ means dimensional variable.

The viscous stress τ_{ij} is defined as follows,

$$\tau_{ij} = \frac{\mu}{Re}\left(\frac{\partial u_j}{\partial x_i} + \frac{\partial u_i}{\partial x_j} - \frac{2}{3}\frac{\partial u_k}{\partial x_k}\delta_{ij}\right), \tag{4}$$

where the dynamic viscosity coefficient is $\mu = \mu^*/\mu_\infty$, the Reynolds number is $Re = \rho^* u_\infty^* L_\infty/\mu_\infty^*$, and δ_{ij} means Kronecker delta. The pressure p depends on gas status equation, and the heat flux q is determined by Fourier heat conduction equation, that is,

$$p = (\gamma - 1)\left(\rho E - \frac{1}{2}\rho u_i u_i\right) = \frac{1}{\gamma M_\infty^2}\rho T, \tag{5}$$

$$q = \frac{-\mu}{(\gamma - 1)M_\infty^2 Re Pr}\frac{\partial T}{\partial x_j}, \tag{6}$$

where $T = T^*/T_\infty^*$, the steady specific heat ratio is $\gamma = 1.4$ and the expression of inflow Mach number is $M_\infty = u_\infty^*/\sqrt{\gamma R^* T_\infty^*}$. The gas constant $R^* = 287\text{J}/\text{Kkg}^{-1}$ and the Prandtl number $Pr = 0.72$.

As the temperature of gas is between 100 and 1900 K, the dynamic viscosity coefficient can be obtained by Sutherland law,

$$\mu^*\left(T^*\right) = \frac{C_1^* T^{*3/2}}{T^* + S^*},$$ (7)

$$C_1^* = \frac{\mu_r^*}{T_r^{*3/2}}\left(T_r^* + S^*\right),$$ (8)

where $S^* = 110.4\text{K}$ for air, and $\mu_r^* = 1.716 \times 10^{-5}\text{kg}/\text{ms}$ is the dynamic viscosity coefficient at $T_r^* = 273.15\text{K}$.

2.2 Physical problem and numerical solution

For 3D flat-plate compressive turbulent boundary layer, the inflow Mach number M_∞ is 0.7 and the inlet Reynolds number $Re_{\delta_d^0}$ is 500 (based on the displacement loss thickness of inlet boundary layer δ_d^0). The size range of the flat-plate in the streamwise direction x, the normal direction y, and the span direction z is $L_x \times L_y \times L_z = 3000\delta_d^0 \times 65\delta_d^0 \times 130\delta_d^0$, which corresponds to the actual length of $30 \times 0.65 \times 1.3$ (inch^3). The spanwise length exceeds 2 times the thickness of the boundary layer δ_{99} (which takes the position with 0.99 times of inflow velocity). The analysis of two-point correlation confirms that this length is sufficient and will not affect the turbulence dynamics. Note here the characteristic length L_∞ in the numerical calculation is 1 inch. The grid for the uncontrolled smooth flat plate is uniformly distributed in the x, z directions, and grows exponentially in the y direction. The number of grid nodes in the x, y, z directions is $2338 \times 160 \times 320$, so that the spatial resolutions in the near-wall region reach $\Delta x^+ = 20.45$, $\Delta y^+ = 0.21$, $\Delta z^+ = 8.39$, which are comparable with resolvent size of spatially developing flat plate turbulent boundary layer in Kametani, Fukagata, Örlü et al. [31] and Xie, Zheng, Zhang, et al. [32] and slightly smaller than that in Schlatter, Örlü, Li, et al. [33]. Note that the superscript $+$ means normalization by the viscous length scale in the wall unit $y^+ = y \cdot \rho_w u_\tau / \mu_w$, where $u_\tau = \sqrt{\tau_w/\rho_w}$ is the wall friction velocity and $\tau_w = \mu_w\left(\partial u/\partial y\right)_{y=0}$. The inlet conditions are $\rho_\infty = 1.0$, $u_\infty = 1.0$, $v_\infty = 0$, $w_\infty = 0$, $T_\infty = 1.0$. The non-slip wall temperature T_w is 1.098, which exceeds the inflow temperature, thus a heated boundary layer will be generated near the wall. The normal boundary and the flow exit boundary are set as non-reflective conditions, and the span direction is periodic boundary conditions.

The calculation procedure adopts the compressible high-order finite difference solver Hoam-OpenCFD developed by Li & Fu [34, 35] from Institute of Mechanics, Chinese Academy of Sciences. The inviscid terms are split by the Steger-Warming flux vector [36]. The convection term and diffusion term are processed by a 7th order upwind scheme and 8th order central difference scheme, respectively, and a three-step 3th order Runge–Kutta method is conducted for time advancement. The setting details of numerical algorithms and calculation models can refer to the previous work [37].

Figure 1 shows the instantaneous density contour at $z = 0.65$ cross-section of the smooth flat-plate turbulent boundary layer. We can see that the compressible free inlet flow transited into spatially developed turbulence through the upstream
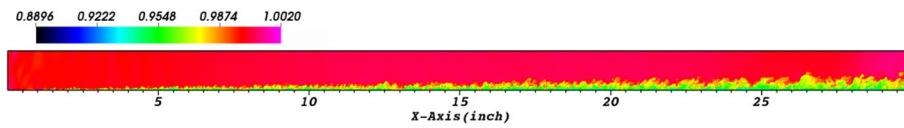
**Fig. 1** Instantaneous density contour at $z = 0.65$ section
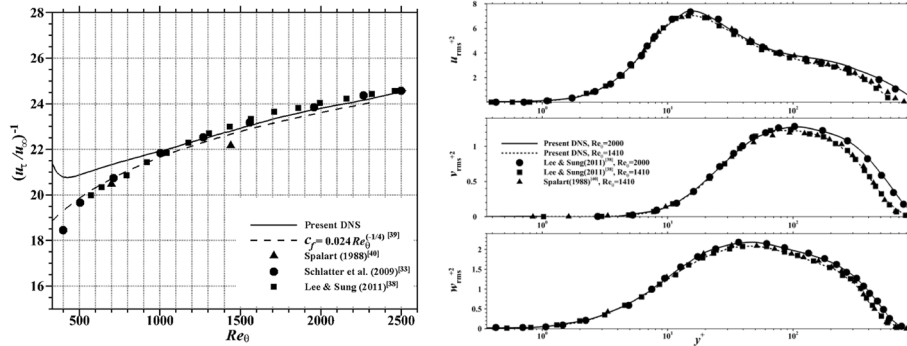
Fig. 2 Profiles of wall friction velocity with momentum Reynolds number (left) and distributions of Reynolds stresses at $Re_\theta = 1410$ and 2000

transition zone ($x < 10$). The density within the boundary layer is less than that of the free flow, and the distribution thickness gradually increases along the downstream development, predicting the increasing thickness of the turbulent boundary layer. Figure 2 illustrates the variation of wall friction velocity along the turbulent momentum Reynolds number Re_θ. Thus, we can see the evolution of the wall friction coefficient c_f ($\sqrt{c_f/2} = u_\tau/u_\infty$) along the smooth flat plate. Note that a local blowing/suction (B/S) control strip on the wall is applied to the region that is close to the inlet. The aim is to accelerate the process of laminar-to-turbulent transition. Thus, the friction velocity near the inlet has a deviation from the references [38–40]. However, in our focus area with spatially developed turbulence $Re_\theta > 1000$, the wall friction decreases slowly with the increase of the downstream turbulent boundary layer thickness. The current DNS results are in good agreement with Schlatter, Örlü, Li, et al. [33] and Lee & Sung [38] turbulent plate boundary layer data, which are slightly larger than the simple empirical equation [39] $c_f = 0.024 Re_\theta^{(-1/4)}$, with relative errors of less than 2%. In addition, the comparisons of turbulent Reynolds stresses at the locations of $Re_\theta = 1410$ and 2000 have shown that the current fluctuation results are consistent with the DNS of Lee & Sung [38]. At two Reynolds numbers, the peak values of the streamwise normal stress (u_{rms}^{+2}) are 7.15 and 7.39 at the location $y^+ \approx 14$. For the wall-normal (v_{rms}^{+2}) and spanwise (w_{rms}^{+2}) normal stresses, the peak locations for $Re_\theta = 2000$ move outward, which are obtained at $y^+ = 115$ and $y^+ = 48$, respectively.

According to the evolution results of smooth uncontrolled flat plate turbulent boundary layer, periodic isosceles triangular riblets are arranged on the flat plate in the direction of flow in the downstream region $x = [22.5, 25]$ (corresponding to smooth flat plate turbulent boundary layer $Re_\theta = [2107, 2332]$), in order to observe the effect of the riblets on the control of drag in the moderate Reynolds number
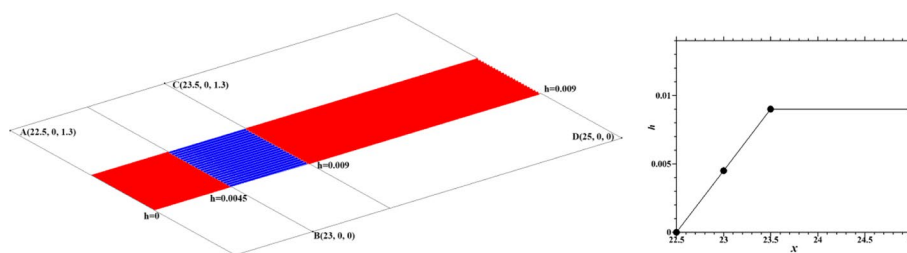
Fig. 3 The flat-plate model with riblets control (left) and the riblets height distribution along streamwise direction (right)
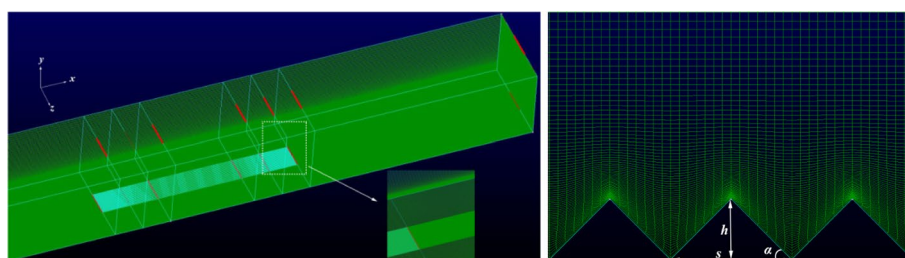

Fig. 4 Schematic of three-dimensional grid (left) and grid distribution near the triangular riblets (right)

turbulent boundary layer flow. In a large number of previous studies [2–5], the optimum drag reduction occurs in the range of $h^+ = 8 \sim 15$. Especially, the sawtooth V-grooves manufactured by the 3M company (USA) have been widely investigated, and the maximum viscous drag reduction can be reached at $4 \sim 8\%$ in mild pressure gradients. However, the effectiveness and degree of drag reduction by riblets are closely related to the geometrical configuration, turbulent states and flight conditions, which are still not fully understood at present. For the exploration of flow mechanism in numerical methods, the smaller the groove, the smaller the mesh size required for fine resolution. In the current DNS study, the triangular riblets with the bottom edge $s = 0.018$, the height $h = 0.009$, $\alpha = 45°$, corresponding to $s^+ \approx 30.82$, $h^+ \approx 15.41$ normalized by the same position of smooth flat plate local viscosity scale ν/u_τ, are shown in Fig. 3. Here, in order to make the transition of the turbulent boundary layer flow field as smooth as possible when encountering the raised riblets, a transition section is arranged in front of the riblets, whose height grows linearly from $h = 0$ to $h = 0.009$. In the area where the riblets control is imposed, the computational grid is locally densified so that each triangle occupies 16 grid nodes on one side and grows vertically along the normal direction of the riblets wall, thus ensuring the orthogonality of the grid near the wall, as shown in Fig. 4. The number of grid nodes is $2338 \times 160 \times 499$ in three directions for the entire 3D riblets-controlled flat-plate domain. The same initial and boundary conditions as in the smooth plate case are used, and the same DNS solver is applied to numerically solve the turbulent boundary layer of the riblets control case.
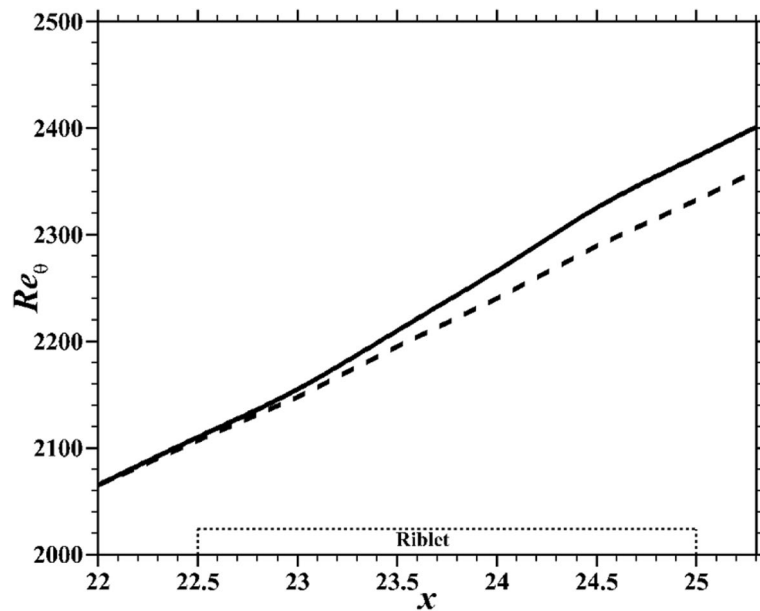
Fig. 5 Spatial development of the boundary-layer momentum Reynolds number Re_θ (The solid and dashed lines indicate the riblets case and smooth case, respectively)
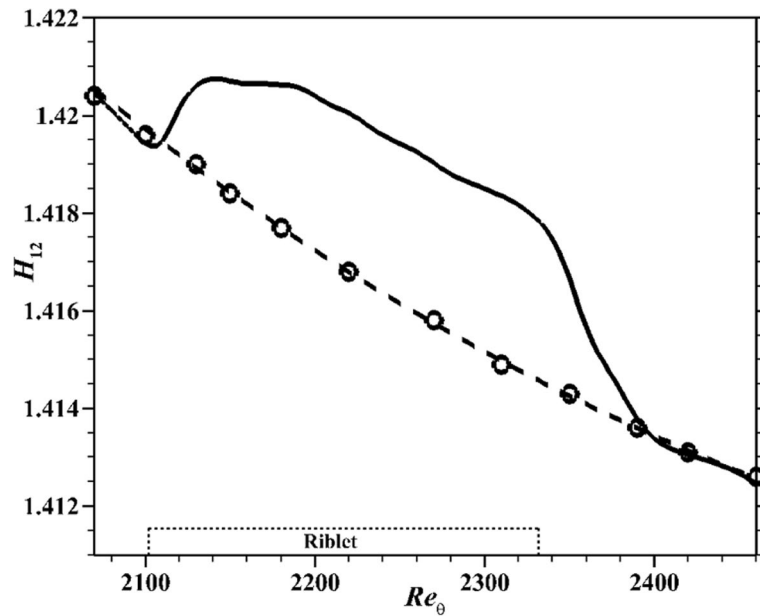
Fig. 6 Spatial development of the boundary-layer shape factor H_{12} (The solid and dashed lines indicate the riblets case and smooth case, respectively. The circle symbol is the results of Schlatter et al. [33]

3 Results and discussions

3.1 Analysis of flow velocity profile and drag reduction rate

The spatial development of the boundary layer along stream-wise x direction in two cases (uncontrolled smooth flat-plate flow; riblets case) is plotted in Figs. 5 and 6. It

shows that the momentum Reynolds number Re_θ grows approximately linearly along the streamwise direction.The riblets control brings about the increase of Re_θ (in the riblets region $x = 22.5 \sim 25$ with black dashed box in Figs. 5 and 6), which indicates the thickened boundary layer. The definition of shape factor H_{12} is the ratio of the displacement thickness δ_d to the momentum loss thickness δ_θ in the boundary layer. The riblets array promotes the shape factor significantly. Before and after riblets array, the shape factor experiences a process of first increasing and then decreasing. When it exceeds the riblets control area, the shape factor and the momentum Reynolds number will quickly return to the same state as that of the uncontrolled case. The larger the shape factor, the less filled the velocity profile, which predicts an enhanced drag reduction, as can be seen from the velocity distribution on the riblets wall.

Figure 7 shows the velocity distribution from the valley to the tip position of the riblets in the boundary layer, where the thickness of the outer layer of the boundary layer δ_{99} is taken as the dimensionless scale parameter and U denotes the time-averaged flow velocity. It can be seen that at $y/\delta_{99} > 0.06$, the average velocity distributions at different locations in the riblets are the same. The area of influence that produces the velocity variation is mainly in the vicinity of the near-wall riblets and the flow velocity is greater at the valley compared to the tip at the same wall normal position y, which is consistent with the experimental observations of Vukoslavcevic, Wallace & Balint [41].

In order to investigate the flow field structure in the inner layer of the boundary layer under riblets control, it is necessary to analyze the mean velocity distribution in the turbulent boundary layer with the wall friction velocity u_τ and the viscous scale ν/u_τ as dimensionless parameters. Figure 8 compares the mean velocity U^+-y^+ variation of the boundary layer for the smooth and riblets-controlled cases, using the local friction velocity u_τ and the viscous scale ν/u_τ at the respective locations of the riblets walls to
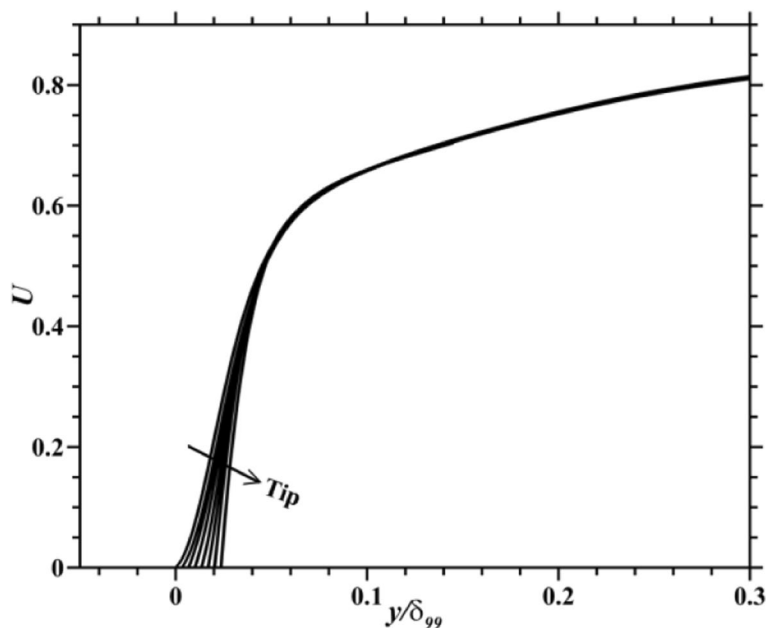
**Fig. 7** Averaged velocity distribution of riblets-controlled case
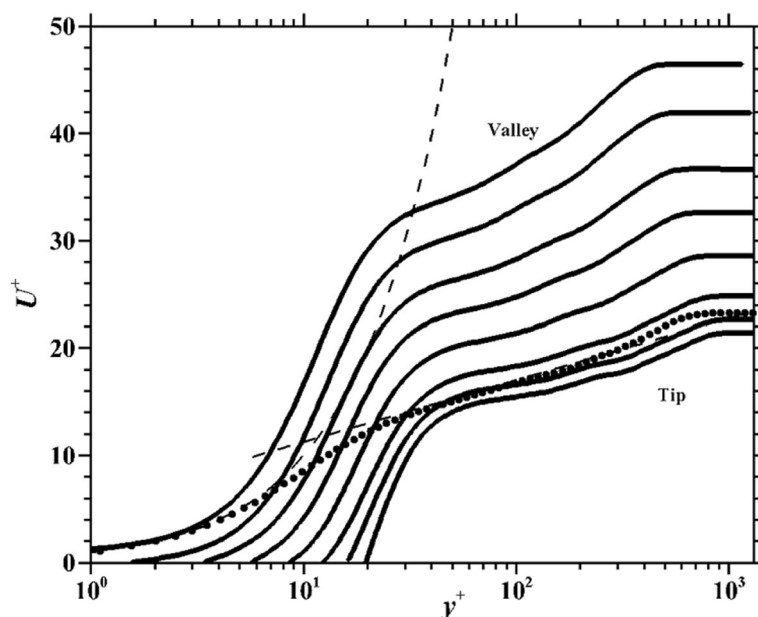
Fig. 8 Van Driest transformed averaged velocity distribution normalized by wall viscous unit

normalize the time-averaged flow velocity U and the wall normal height y. The dots and solid lines in the figure indicate the velocity distribution curves of the turbulent boundary layer of smooth and trench flat plates, respectively, and the two dashed lines are the linear wall law $U^+ = y^+$ and logarithmic law curves $U^+ = 2.5\ln(y^+) + 5.5$, respectively. It can be seen that the log-law curves of the turbulent boundary layer at different positions from the valley to the tip of the riblets have different degrees of upward or downward shifts compared to the smooth flat-plate case, resulting in differences in the velocity magnitude of outer boundary layer U^+. Among them, the log-law curve is shifted downward near the wave peak position, and the maximum velocity of the outer boundary layer ($U^+ \approx 21$) is smaller; The log-law curve at the valley is shifted upward and its maximum velocity in the outer boundary layer reaches a maximum value of $U^+ \approx 46$. The upward or downward deviation of the log-law curve and the variation of the magnitude of the outer boundary layer velocity U^+ characterize the difference in the friction velocity u_τ of the turbulent boundary layer, which leads to the difference in the friction drag on the surface of the flat-plate.

Due to the very small scale of the riblets, it is often difficult for the probe to penetrate into the riblets in engineering experiments, which makes it difficult to determine the wall friction. This involves the selection of the virtual origin of the wall and the determination of the friction velocity. In the numerical simulation of this paper, the tip and valley positions of the riblets are selected as the virtual origin of the riblet wall, and the average velocity profile distribution above the riblets is thus obtained, as shown in Fig. 9. Note that the curves do not include the viscous sublayer data because the velocity distribution of the viscous sublayer varies in the riblets spreading direction for different virtual origin conditions.

In contrast to the velocity profile of the turbulent boundary layer of a smooth flat plate at the same position of the flow direction ($Re_\theta = 2320$, $Re_\tau = 500$), the slope of the
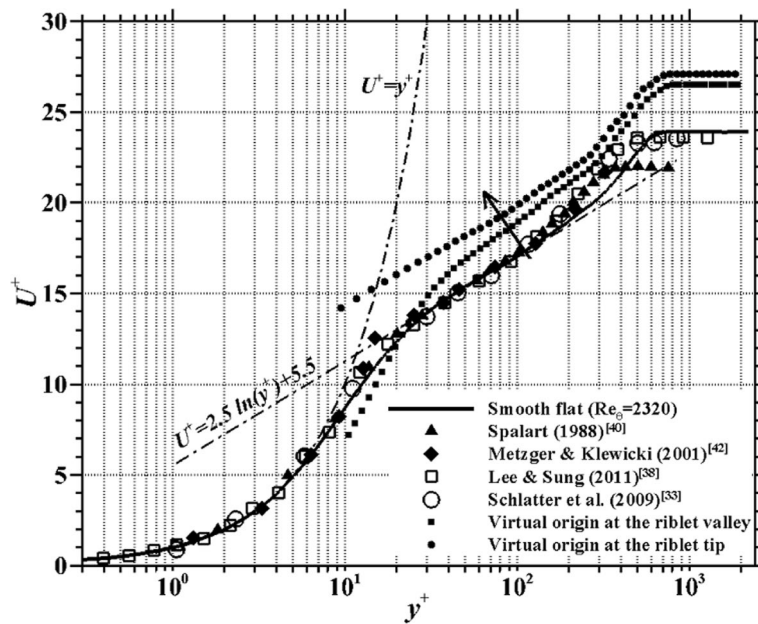
Fig. 9 Comparison of Van Driest transformed averaged velocity profiles in wall viscous units [33, 38, 40, 42]

logarithmic law of the turbulent boundary layer changes very little and rises upward regardless of whether the virtual origin is chosen at the tip or the valley of the riblets. This indicates that the current configuration of the riblets brings about an increase in the thickness of the viscous sublayer at the wall and a decrease in the wall friction velocity, which lead the riblets control to a drag reduction effect. Luchini, Manzo & Pozzi [3], Choi, Moin & Kim [18], Park & Wallace [43] and Wang, Lan & Chen [44] also believe that the low-velocity fluid inside the riblet increases the thickness of the viscous sublayer of the boundary layer, which moves the buffer layer and log-law layer outward, and the fluid momentum and energy exchange near the wall are weakened after the boundary layer is elevated, which reduces the wall shear stress.

Based on the relationship equation of the wall local friction coefficient c_f, the riblets-controlled drag reduction rate DR of the flat-plate turbulent boundary layer flow is defined as follows:

$$c_f = \frac{\mu_w \, \partial u / \partial n \big|_w}{0.5 \rho_\infty u_\infty^2}, \tag{9}$$

$$DR = \frac{\int_{A_f} c_{f0} - \int_{A_r} c_f}{\int_{A_f} c_{f0}}, A_f = A_r \cos \alpha, \tag{10}$$

where c_{f0} and c_f denote the friction coefficients of smooth and riblets-controlled flat plates at the same position, respectively, and A_f and A_r are the corresponding areas of the two cases.

In Fig. 10, the spatial development of the local friction drag coefficient shows the different drag-reduction effect by the current riblet configuration. Inside the riblet, the skin friction drag decreases in the comparison of the smooth flat-plate case, and it reaches
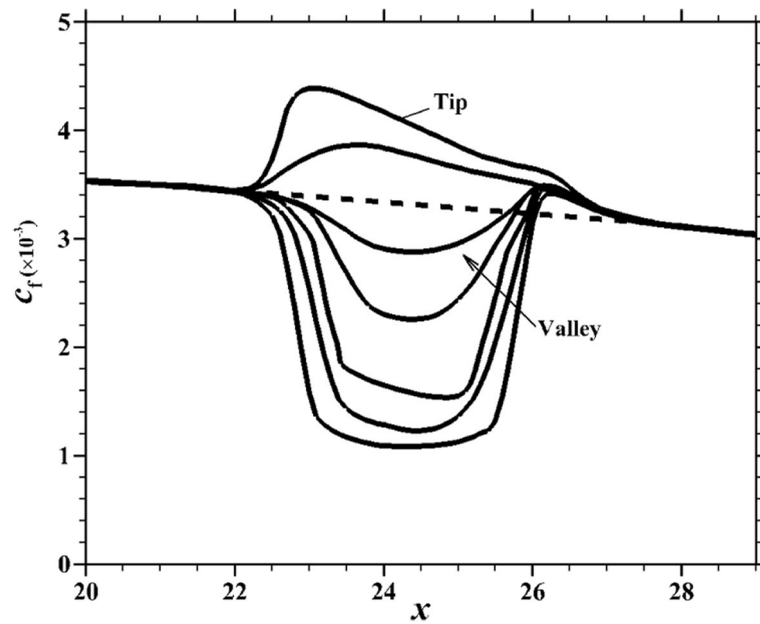
Fig. 10 Streamwise development of local friction drag coefficient on riblets (solid lines) and smooth (dashed line) flat-plate cases
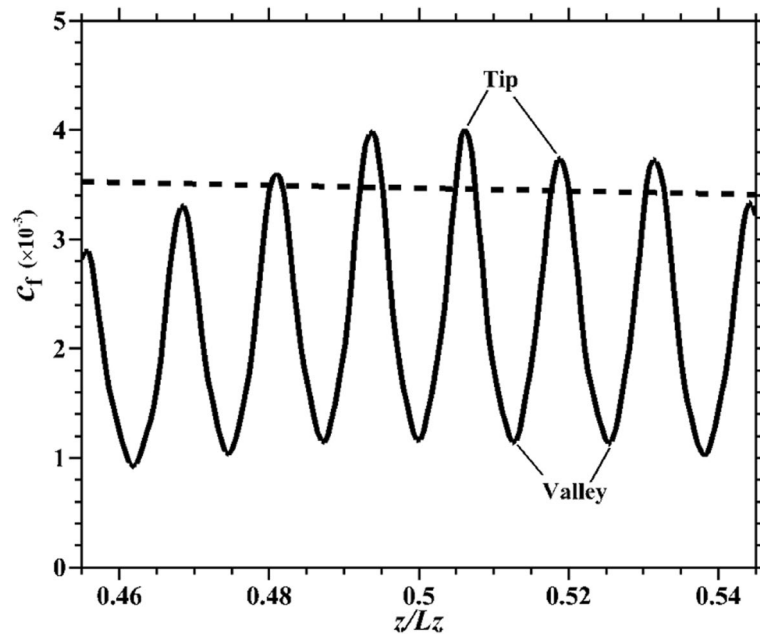
Fig. 11 Spanwise distribution of local friction drag coefficient on riblets (solid lines) and smooth (dashed line) flat-plate cases

the minimum at the valley position. Gradually upward from the valley, the skin friction drag starts to grow and exceed the basic friction drag, and finally reaches the maximum at the tip position. It shows the drag reduction is not available at any position of the riblet. Especially at the tip, the boundary layer might be enhanced in the loss of groove

cavity protection. Similarly, after the riblets area, the local skin friction drag quickly recovered to be consistent with the smooth flat-plate case.

The spanwise distribution of the local friction drag coefficient at the riblet location (corresponding to the smooth flat plate $Re_\theta = 2320$) is given in Fig. 11. It can be seen that since the riblets are periodically arranged in the spanwise direction, the variation of the local friction coefficient is also periodic. However, it is worth noting that there is a small difference in the magnitude of their fluctuation amplitudes. This is due to the fact that the riblets array does not fill the entire flat plate spanwise space, and the riblets-controlled turbulence boundary layer is affected by the smooth area flow field when approaching the edge position of the controlled region. At the same time, the wall friction reaches the maximum and minimum values at the tip and valley of the riblets, respectively, which indicates that the riblets valley acts as a natural depression barrier zone that facilitates the accumulation of low-speed airflow with a larger viscous sublayer thickness than the tip position.

In comparison with the wall local friction of smooth flat-plate case, the wall local friction coefficients of most positions on the riblets are smaller than those calculated from smooth plate, except for the tip positions of the riblets, which is slightly larger than that of the smooth flat-plate case at the same position. In order to investigate the drag reduction effect of riblets control on the turbulent boundary layer of the entire flat-plate wall surface, the area integral of the wall local friction is performed. Note that the wetted area of riblets plate is $1/\cos(\alpha)$ times larger than that of the flat plate, see Eq. (10). Thus, the plane- and time-average drag reduction can be obtained as the integral of wall friction coefficient on the wetted area. This results in a global drag reduction rate DR of 1.276% for the current riblets configuration ($s^+ \approx 30.82$, $h^+ \approx 15.41$), which is close to the value of 1.2% from Bechert, Bruse, Hage, et al. [4].

3.2 Analysis of velocity fluctuation field

In order to visualize the effect of the riblets on the turbulent structure evolution process, the flow fluctuation velocity u' distribution of the spatially fully developed flat-plate turbulence from the smooth region to the riblets region and the downstream flow field is shown in Fig. 12. The dashed box is the riblets-controlled region, and the three normal cross sections correspond to the buffer layer ($y^+ = 8.43$, 20.35) and
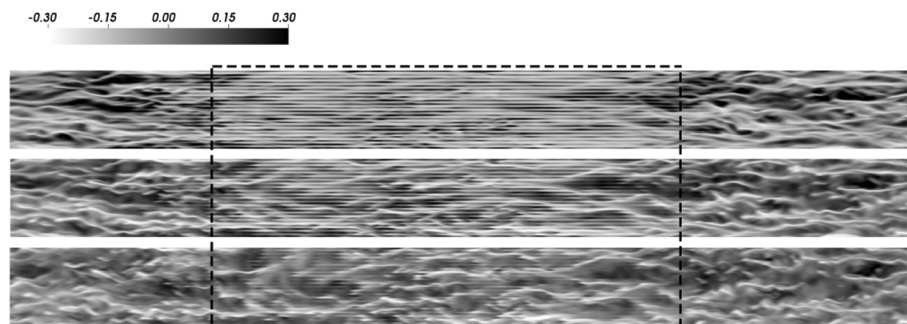
Fig. 12 Fluctuation velocity u' distribution at three cross-sections. (The top, middle and bottom correspond to $y^+ = 8.43$, 20.35, 39.22, respectively, and the dashed box is the riblets control area)
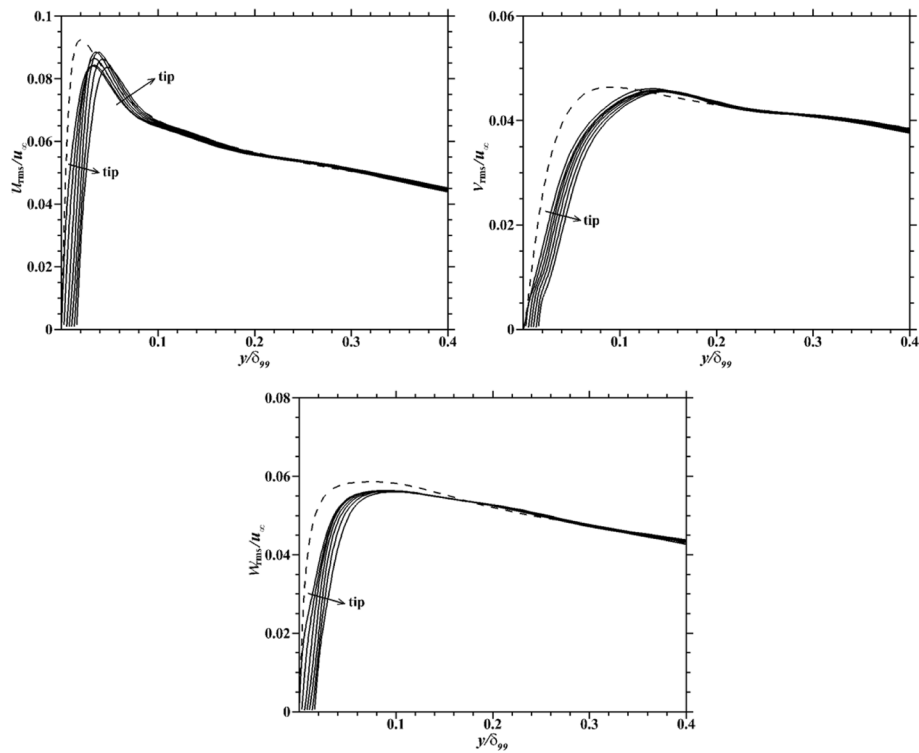
Fig. 13 Wall turbulence fluctuation Root Mean Square (RMS) distribution. (The dashed line indicates the result of the smooth flat-plate case, and the arrow marks the position from the valley to the tip of riblets)

the log-law layer ($y^+ = 39.22$) of the turbulent boundary layer, respectively. Here, the viscous scale of the wall at $x = 20$ in front of the riblets is taken to be dimensionless.

It can be clearly seen that distorted turbulent fluctuation streaks fill the smooth region in front of and behind the riblets region near the wall buffer layer $y^+ = 8.43$. As these structures flow through the riblets area, they are divided into a straight and elongated structure that flows neatly and orderly downstream along the riblets channel. After passing through the riblets area, the straight streaks structure starts to become distorted again. In addition, as it gradually moves away from the wall $y^+ = 20.35$, the straight streaks above the riblets gradually start to deform and distort. At $y^+ = 39.22$, the turbulent fluctuation structures in the smooth region before and after the riblets and in the riblets region are basically similar. This shows that the riblets have a strong rectification effect on the turbulent fluctuation structure in the near-wall region, but this rectification effect will gradually weaken along the normal direction of the wall until it finally disappears. This shows that the effect of the current micro-scale riblets on the turbulent boundary layer flow field at the wall is limited to the near-wall region.

As Fig. 13 quantifies and compares the root mean square (u_{rms}, v_{rms}, w_{rms}) distribution of turbulent fluctuation from the valley to the tip inside the riblets, where the riblets position in the streamwise direction is chosen to correspond to the smooth flat plate at $Re_\theta = 2320$, and the dashed line is the result of the smooth flat-plate case. It can be seen that, regardless of the riblets or smooth flat-plate case, the flow direction

positive stress is the largest among the three directions of Reynolds positive stress, that is, the streamwise turbulent fluctuation intensity is the largest.

The maximum value of u_{rms} in the smooth flat-plate case is obtained at $y/\delta_{99} \approx 0.018$ (corresponding to $y^+ \approx 15$). Comparing it with the turbulent fluctuation field after applying the riblets control shows that the fluctuation peak is obtained at a position elevated outward the wall. At the same time, the peak magnitude also decreases relative to the smooth flat-plate case, indicating that the turbulence intensity above the riblets decreases after the riblets control is applied. Comparing the turbulent fluctuation intensity at different positions inside the riblets, it can be found that the turbulent fluctuation intensity decreases from the valley to the tip of the riblets in all three directions at the same normal wall position y. However, beyond the peak point, the turbulent fluctuation variations at the tip and valley converge quickly. It is worth noting that the maximum value of turbulent streamwise fluctuation u_{rms} inside the riblets is not obtained at the tip or valley of the riblets, but somewhere between them. Despite this, the maximum value is still smaller than the peak turbulent fluctuation of the smooth flat-plate case.

Quadrant analysis of Reynolds shear stress according to the sign of u' and v' is good for understanding the evolution of turbulent kinetic energy production caused by riblets in the boundary layer. The first ($u' > 0$, $v' > 0$) and third ($u' < 0$, $v' < 0$) quadrant events contribute to negative turbulent kinetic energy production, and the second ($u' < 0$, $v' > 0$; ejection) and fourth ($u' > 0$, $v' < 0$; sweep) quadrant events contribute to positive production. Figure 14 shows that the contribution to the Reynolds shear stress $-\overline{u'v'}/u_\infty^2$ from the second quadrant is the largest in the near-wall region from all four quadrants, which means the dominance of ejection event. At the riblet tip, midpoint and valley, all Reynolds shear stress from the ejection event (second quadrant) is reduced in the comparison of the smooth flat case. From the valley to the tip, the maximum value increases a little successively and their peak locations have a little outward shift. For the Reynolds shear stress of sweep events (fourth quadrant), there is a little decrease inside the riblet in the near-wall boundary layer. At $y/\delta_{99} > 0.1$, the value of the smooth flat-plate case becomes a little smaller than that of the riblet flat-plate case, but quickly converges. For the first and third quadrant events, their negative contributions to the turbulent kinetic energy production are small in value relative to the ejection and sweep events. Moreover, the value of the Reynolds shear stress for both smooth and riblet flat cases has no significant change in the whole boundary layer except for a slightly fluctuation at $y/\delta_{99} < 0.06$. Figure 15 shows the contour distributions of Reynolds shear stress $u'v'$ at two moments. The black dashed line denotes the height of the riblet tip. It is observed that there are a few eddies of greater intensity with large $-u'v'$ below the dashed line for the smooth flat-plate case, but almost no eddies inside the riblet. It is because the riblet not only acts as a barrier to the large-scale shear eddies, but also attenuates the ejection and sweep events. Thus, the interaction between the near-wall eddies and the wall under the influence of riblets is weakened.

3.3 Vorticity fluctuation distribution

Figure 16 compares the distribution of streamwise vorticity fluctuation w_x' at different moments of the y–z cross section in the riblets region ($x = 24.12$) for the smooth and riblets-controlled flat-plates cases. It can be seen that the streamwise vorticity fluctuation
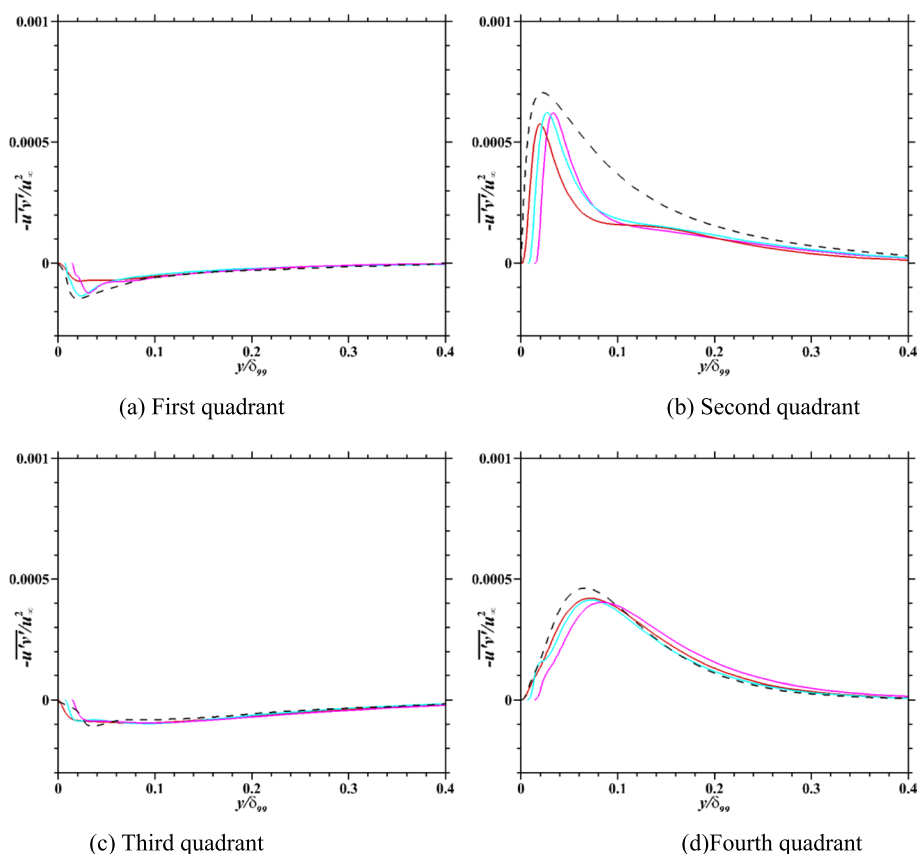
Fig. 14 Reynolds shear stress $-\overline{u'v'}/u_\infty^2$ from each quadrant (The dashed line indicates the smooth flat-plate case and the red, blue and pink colored lines indicate the results in the locations of riblet valley, midpoint and tip). **a** First quadrant. **b** Second quadrant. **c** Third quadrant. **d** Fourth quadrant

at the smooth flat plate case is moving close to the wall, while most of the streamwise vortices in the riblets cross-section appear above the riblets tips. This is related to the size of the riblets: when the riblets size cannot accommodate the streamwise vortices, the streamwise fluctuation vortices cannot interact directly with the riblets wall, so the shear stress on the wall decreases. Since the tip position can directly contact with the streamwise fluctuation vortices, the intensity of the streamwise fluctuation vortices at this position is also numerically significantly higher than that of other positions in the riblets.

Figure 17 quantifies the magnitude of the streamwise vorticity fluctuation inside the riblets, where $|w_x'|$ takes the average of all the streamwise vorticity fluctuation at each observation point 1–5 inside the riblets at the spanwise corresponding positions. When the riblets control is applied, the peak of the streamwise vorticity fluctuation in the turbulent boundary layer decreases and the position of the peak point moves out of the wall when compared to the smooth flat-plate case. When $y/\delta_{99} > 0.1$, the vorticity fluctuation distribution inside the riblets is slightly larger than that of the corresponding position of the smooth flat-plate case. At this time, the streamwise vorticity fluctuation along the normal direction of the wall has begun to show a decreasing trend, which indicates that micro-scale riblets lift up the streamwise vortex, weakening the intensity of
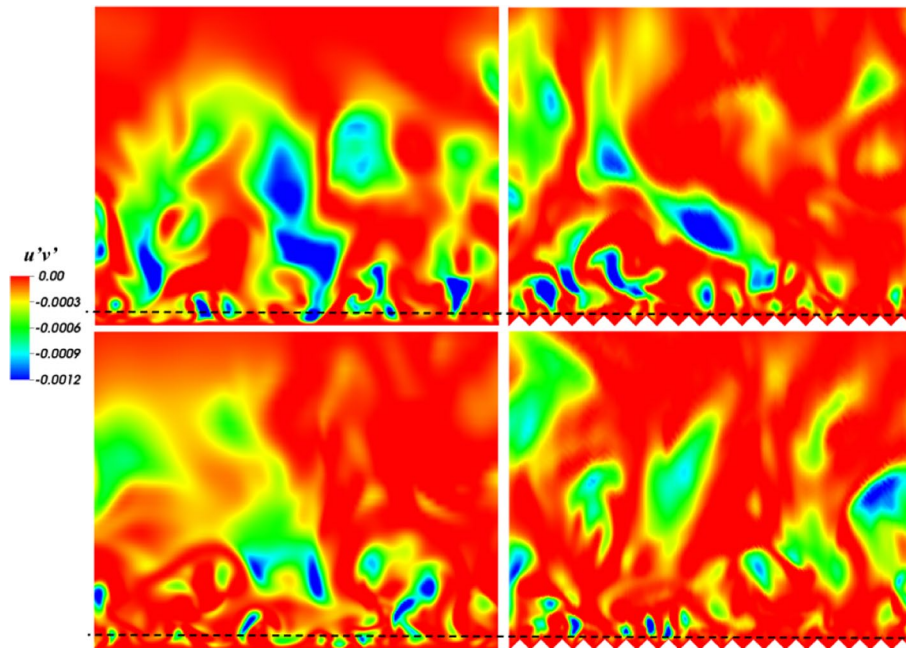
Fig. 15 Contour distributions of $-u'v'$ (The top and bottom represent two moments respectively)

the streamwise vorticity fluctuation in the near-wall area, but the intensity of the streamwise vorticity fluctuation in the outer layer of the boundary layer away from the wall increases slightly. In addition, it was found that the peak of the streamwise vorticity fluctuation tends to increase gradually from the valley to the tip (positions 1 to 5), with the smallest value of vortex pulsation at the valley position.

The distributions of the wall-normal vorticity fluctuation w_y' are given in Fig. 18. Comparing with the results of the smooth flat-plate case, it can be seen that a pair of wall-normal vortices with opposite positive and negative values appears on both sides of almost each riblets tip, which are more neatly arranged in the whole spanwise riblets
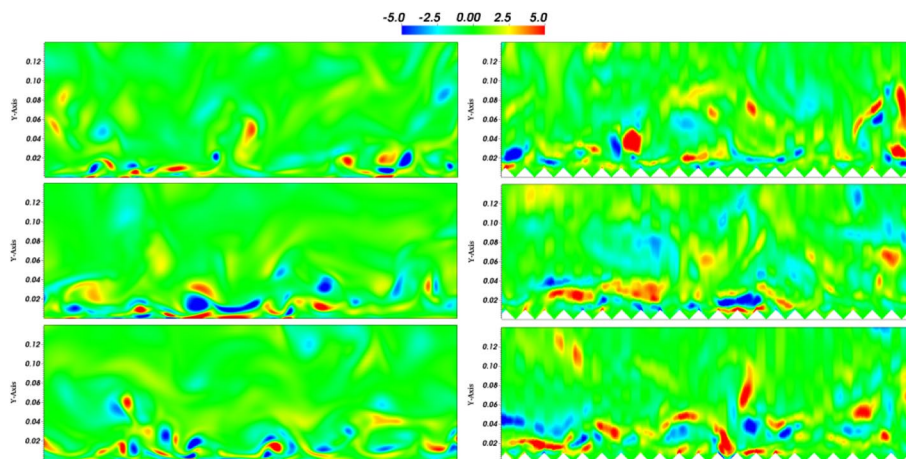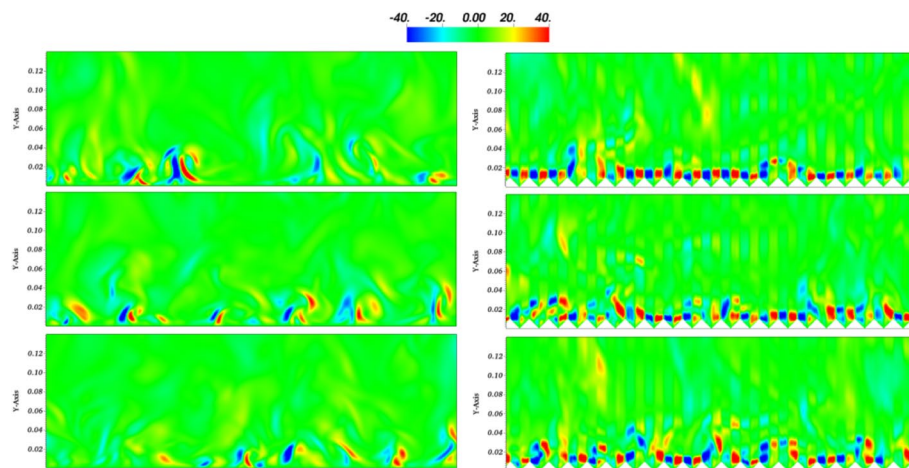

Fig. 16 Distribution of streamwise vorticity fluctuation w_x' in three moments (Left: smooth flat-plate case; Right: riblets-controlled case)
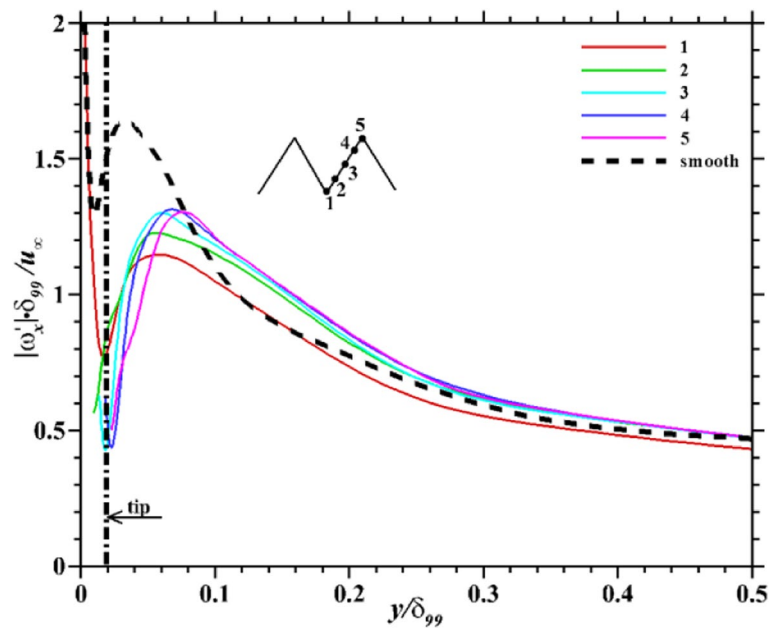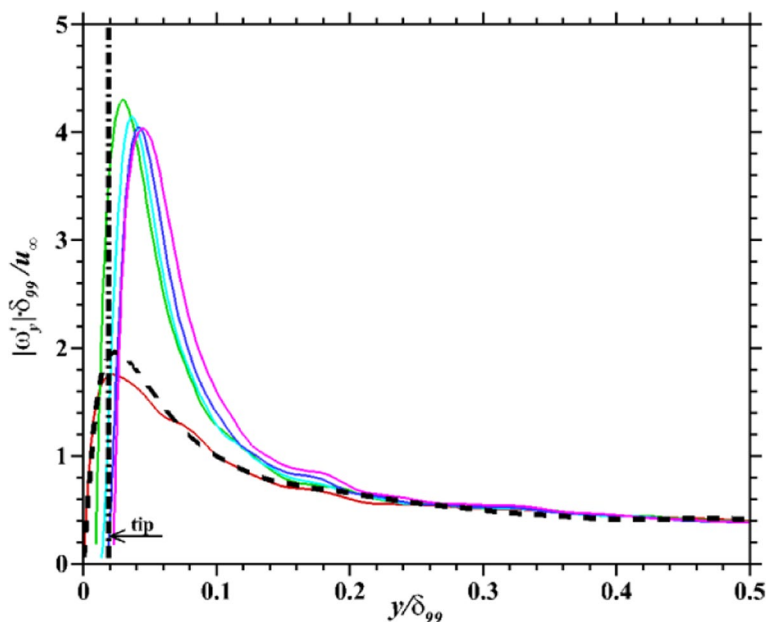
Fig. 17 Quantitative distribution of streamwise vorticity fluctuation

array space, while the wall-normal vortices of the smooth flat-plate case are also presented in the form of pairs, but the distribution is more scattered.

Figure 19 quantifies and compares the wall-normal vorticity fluctuation distribution for both smooth and riblets flat-plates case. It can be seen that when the riblets control is applied, the wall-normal vorticity fluctuation magnitude increases significantly and the peak point location is slightly higher than that of the smooth flat plate case. In addition, the maximum value of the wall-normal vorticity fluctuation is not obtained at the tip position because the wall-normal pairs of vortices are distributed on both sides of the tip. The value of $|w_y'|$ decreases from position 2 to tip position 5, but the overall value is still larger than that of the smooth flat-plate case at the corresponding position.
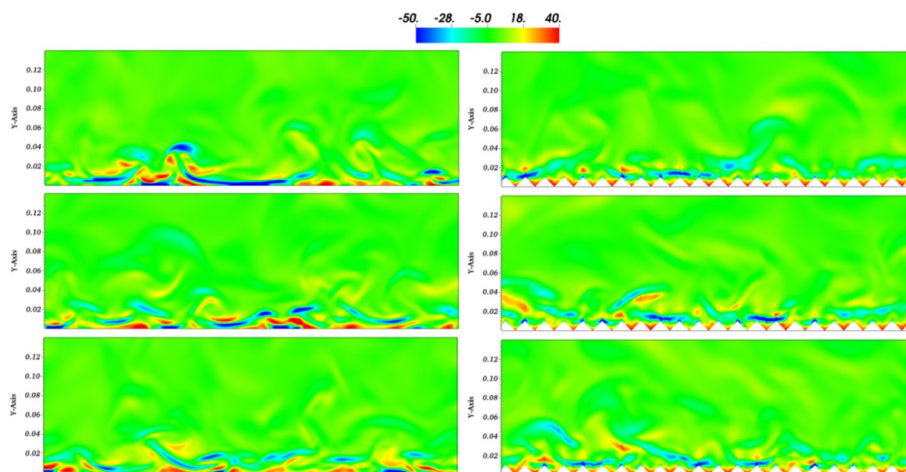

Fig. 18 Distribution of wall-normal vorticity fluctuation w_y' in three moments (Left: smooth flat-plate case; Right: riblets-controlled case)
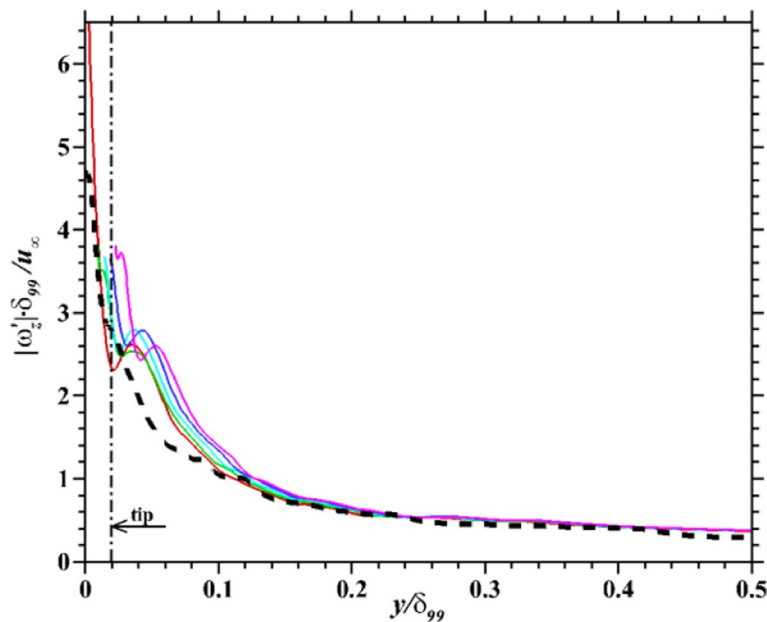
Fig. 19 Quantitative distribution of wall-normal vorticity fluctuation

Figure 20 provides a comparative analysis of the distribution of the spanwise vorticity fluctuation for riblets control. It can be found that the spanwise vorticity fluctuation on a smooth flat-plate case is slimmer in shape than that in both streamwise and wall-normal directions, and the intensity of the spanwise vorticity fluctuation gradually decreases along the wall outward the wall-normal direction. When the riblets control is applied, the vorticity fluctuation inside the riblets is no longer distributed monotonically decreasing along the wall direction, but first decreasing, then increasing and finally decreasing (see Fig. 21). In both near-wall and outer boundary layer regions, the spanwise vorticity fluctuation amplitude is generally larger than that of the smooth flat-plate case.

Table 1 specifically gives the comparison of the peak magnitude and maximum wall-normal offset of the vorticity fluctuation in three directions for both smooth and

Fig. 20 Distribution of spanwise vorticity fluctuation w_z' in three moments (Left: smooth flat-plate case; Right: riblets-controlled case)

Fig. 21 Quantitative distribution of spanwise vorticity fluctuation

riblets-controlled flat-plates cases. It can be seen that due to the existence of riblets, the peak point of vorticity fluctuation in all three directions is raised outward in different degrees, and the magnitude of streamwise vorticity fluctuation is reduced by 20%, which is consistent with the conclusions of numerical simulation from Choi, Moin & Kim [18]. The difference is that the wall-normal vorticity fluctuation obtained from the simulations in this paper increased by 109% compared to the smooth plate case, but the wall-normal vorticity fluctuation simulated in the literature [18] was slightly reduced compared to the smooth plate case. This may be related to the form of vorticity fluctuation processing, where the vorticity fluctuation w' is calculated by first taking the absolute value and then averaging the results in the spanwise direction. Since the wall-normal vorticity fluctuation is closely presented in the form of positive and negative pairs of vortices in each riblets area, its vorticity fluctuation value will become cumulatively larger after the absolute value averaging process.

The existence of the microscale riblets structure makes the turbulent coherent structure in the near-wall region change, in which the lift of the vorticity distribution plays a great role. As stated by Dean & Bhushan [16], most of the near-wall vortices are present above the riblets and their influence area is confined to the tip of the riblets. This is consistent

Table 1 Comparison of the peak magnitude and position of the vorticity fluctuation in three directions

Peak magnitude and maximum offset	symbol	*x*-direction	*y*-direction	*z*-direction
Smooth flat-plate case	$|w'| \cdot \delta_{99}/u_{\infty}$	1.65	2.05	——
Riblets flat-plate case		1.32	4.28	2.78
Incremental percentage		-20%	+109%	——
Smooth flat-plate case	y/δ_{99}	0.033	0.024	——
Riblets flat-plate case		0.082	0.052	0.061
Wall-normal offset	$\Delta y/\delta_{99}$	+0.049	+0.028	——

with Choi, Moin, & Kim [18] and Martin & Bhushan [13, 14] who suggested that the riblet acts as a lift up of streamwise vortex. The streamline distribution of the flat-plate turbulent boundary layer in the y–z section is shown in Fig. 22. It can be clearly observed that the streamwise vortices move close to the wall of the smooth flat-plate, and the intensity of the streamwise vortex in the near-wall area is also larger compared to the riblets-controlled one. Due to the barrier effect of the riblets, large-scale streamwise vortices cannot enter inside the riblets, resulting in a smaller amount of streamwise vorticity inside the riblets.

3.4 Streak structures in the near-wall region

The previous analysis of the riblets flow fluctuation field shows that the rectification of the riblets splits the inner boundary layer flow into a spanwise periodic wall turbulence structure. The streamwise fluctuating turbulence can only flow in an orderly direction along the geometric expansion of the riblets, which limits the spanwise fluctuation of the turbulent flow. At the same time, the flow vortex cannot interact with the near-wall viscous bottom layer due to the lift up effect of the periodic riblets structure, which makes the direct effect of the streamwise vortices on the wall greatly weakened, and thus realizes the effect of wall-bounded turbulence drag reduction. As already pointed out in the analysis of the wall-bounded turbulence velocity profile, the role of the riblets is to lift the velocity distribution in the logarithmic region of the boundary layer upwards as a whole.

In order to visualize the evolution of the turbulent streaks in the near-wall region under riblets control, the three-dimensional contour surface distribution of the transient streamwise velocity of the flat-plate turbulence from the smooth region to the riblets region is shown in Fig. 23. It can be seen that when the flow velocity u is low (e.g., $u = 0.06$), the distribution of velocity iso-surfaces in the smooth region is relatively uniform, while the velocity contour surfaces in the riblets region are distributed in straight streaks, similar to the flow of low velocity fluid downstream along the riblets channel. When the flow velocity increases to 0.1, a few ripples appear on the velocity contour surface in the smooth region, indicating fluctuations and instability in the low velocity fluid, while the velocity distribution remains neat streaks on the riblets region and is not affected by upstream velocity fluctuations. When $u \geq 0.3$, the flow velocity becomes more turbulent on the iso-surface regardless of the smooth
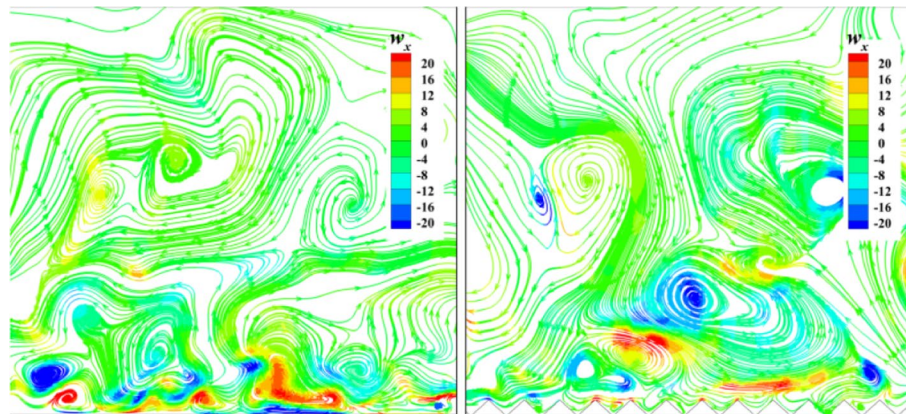
Fig. 22 Streamline distribution at y–z cross-section. (The color indicates the magnitude of the streamwise vortex w_x)
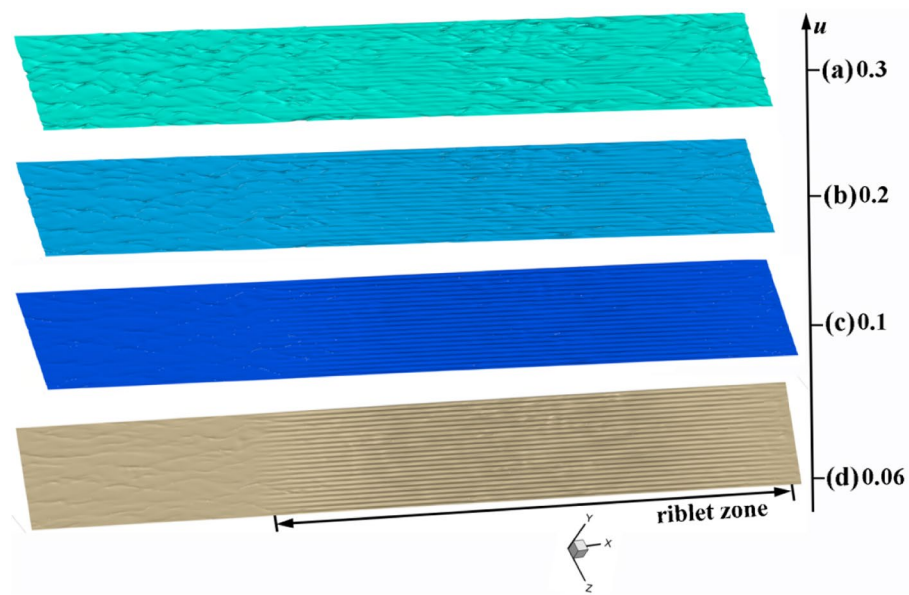
**Fig. 23** Three-dimensional iso-surface distributions of streamwise velocity *u*

area or the riblets area, and the influence of the ribelts on the flow velocity gradually becomes weaker. This indicates that the effect of the riblets is limited to the low velocity fluid near the wall, and makes the low velocity fluid flow along the riblets channel in an orderly manner, thus playing a rectifying role.

This can also be seen in the transient streamwise velocity distribution at *x–z* section shown in Fig. 24. The contour distribution in the near-wall area has many distorted streaks, but after the riblets area the streaks become slender and straight, which forms a sharp contrast with the flow field in the surrounding uncontrolled area. It is also noted that in the downstream region after the riblets control, the thin straight streaks do not immediately return to the turbulent distorted state as before the control region, but extend some distance downstream before finally gradually becoming a distorted and turbulent streak structure. Comparing the magnitude of the transient velocity *u* in the two cases, it can be found that the flow velocity *u* in the riblets area is significantly smaller than that of the smooth flat-plate case at the same location. This indicates that the riblets array provides a good "safe haven" for the low velocity fluid, which is conducive to the slow formation and accumulation of low velocity fluid. The velocity gradient in the middle of the riblets is lower than that in the smooth flat-plate case, implying a lower wall shear stress and therefore a drag reduction effect.

In the spanwise *z*-direction, the two-point correlation function $R_{u'u'}$ with the streamwise velocity fluctuation can express the spanwise length scale of low-speed streaks. It is defined as follows,

$$R_{u'u'}(\Delta z) = \frac{\overline{u'(x,y,z)\,u'(x,y,z+\Delta z)}}{u_{\text{rms}}^2} \tag{11}$$

and the streak spacing λ^+ is twice the spanwise distance, at which the two-point correlation reaches a minimum. Figure 25 presents the distributions of spanwise two-point correlations at $y^+ = 8.43$, 20.35 and 39.22. The streak spacing obtained from the two-point
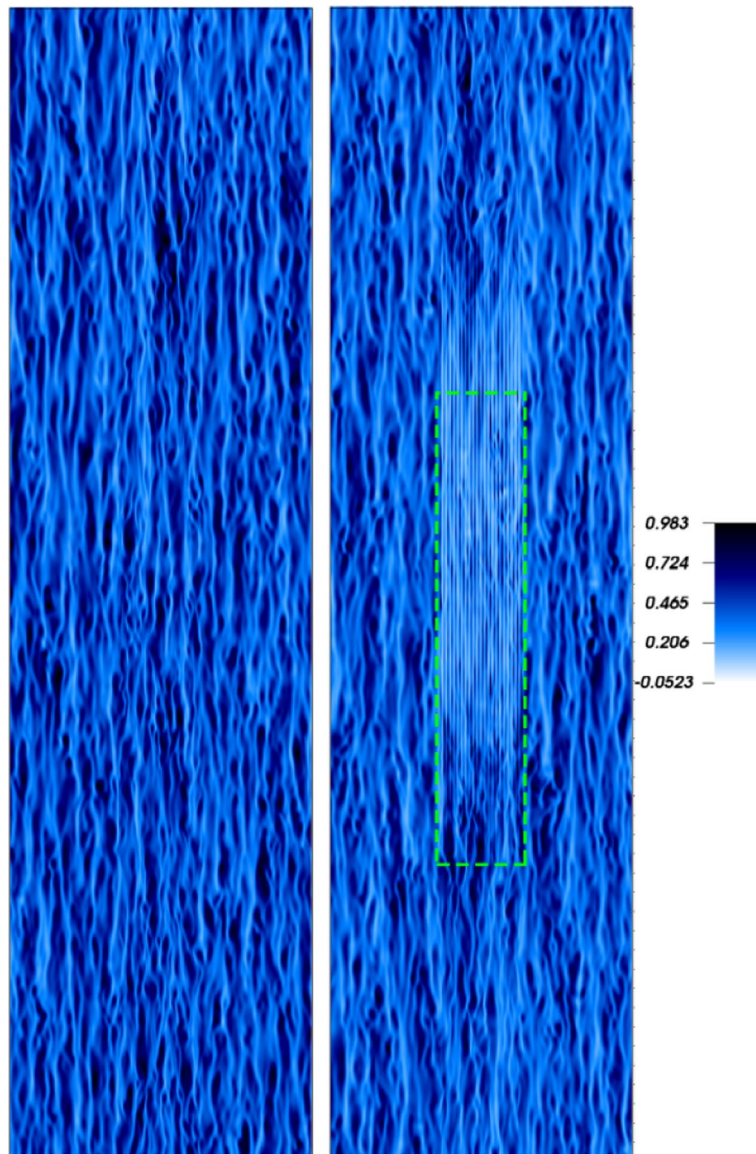
Fig. 24 Instantaneous velocity *u* distribution at *x–z* section of $y^+ = 8.43$. (left: smooth flat-plate case; right: riblets flat-plate case; green dashed box: riblets area)

correlation for both the riblet case and the smooth case is basically at the same level. At $y^+ = 8.43$, it yields 93.0 for the riblet wall and 95.3 for the smooth wall. It can be seen that the streak spacing by riblets control is slightly reduced, but not much, indicating that the spanwise streak spacing is less affected by riblets. As it moves away from the wall from $y^+ = 8.43$ to $y^+ = 39.22$, the streak spacing gradually increases. Moreover, the two-point correlation will gradually tend to 0 at an increasing Δz^+, which is due to the decrease of streamwise fluctuation in correlation.

The distributions of the three-dimensional iso-surface for the second-order invariant for the velocity gradient tensor $Q_2 = 20$, 50, 80, 110 in both riblets-controlled and smooth-plate cases are given in Figs. 26 and 27. The color indicates the magnitude of the instantaneous velocity *u*. The green box indicates the area where the
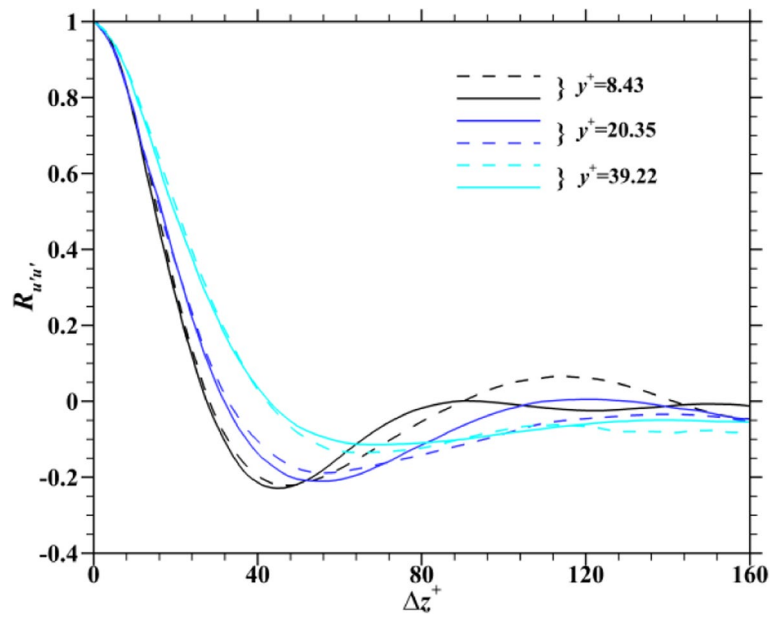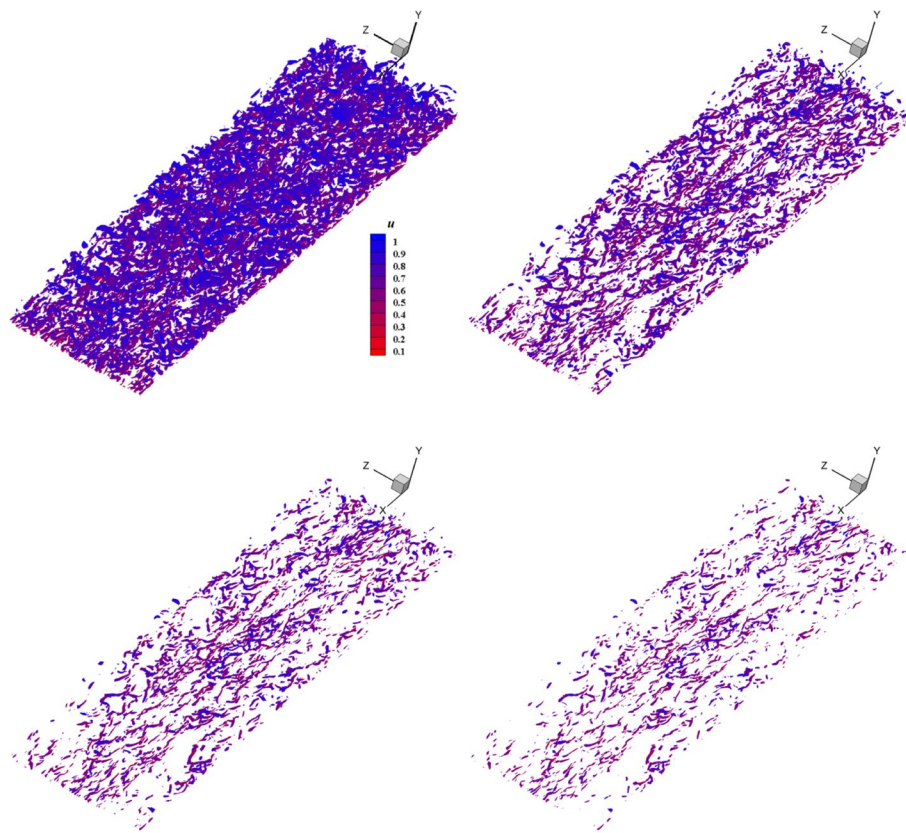
Fig. 25 Distribution of two-point correlations in the span-wise direction at different heights from the wall (solid: riblet case; dash-dot: smooth case)
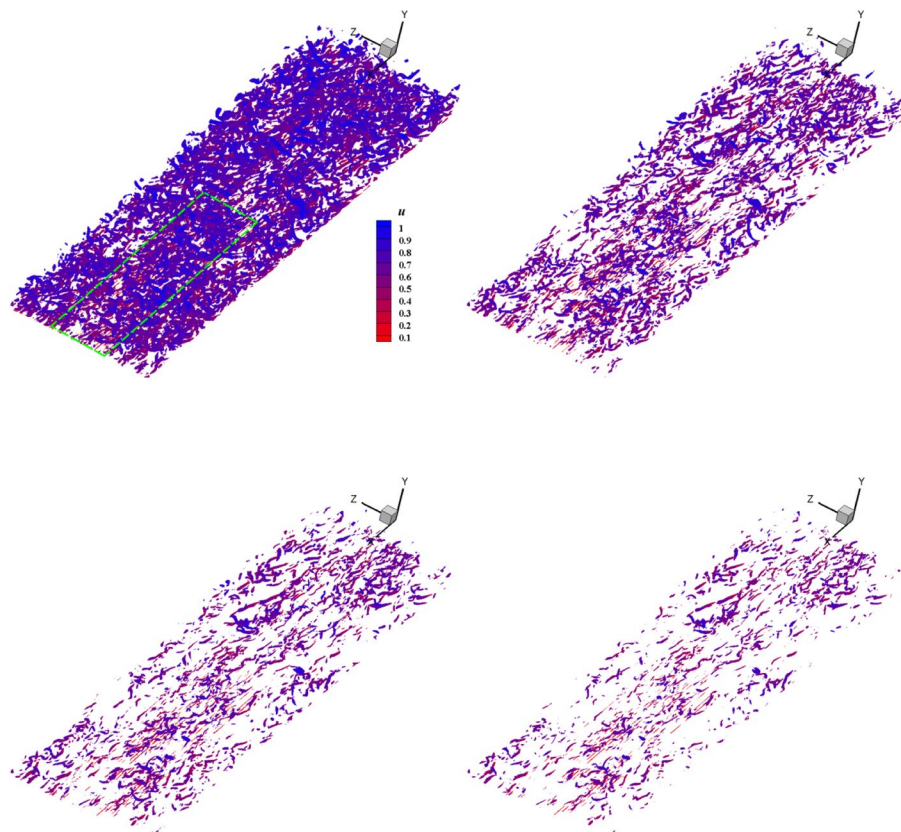
Fig. 26 The second-order invariant of the velocity gradient tensor Q_2 in the riblets case (From top-left to bottom-right: $Q_2 = 20, 50, 80, 110$)

Fig. 27 The second-order invariant of the velocity gradient tensor Q_2 in the smooth-plate case (From top-left to bottom-right: $Q_2 = 20, 50, 80, 110$)

riblets are located. It can be seen that the 3D vortices gradually become less as the Q_2 increases. For those 3D vortices in the near-wall region, their shapes are pulled long and straight as they pass through the riblets region. In an orderly manner, those 3D vortices move along the riblet array in the streamwise x-direction. The streamwise velocity of those straight 3D vortices is smaller than that of the surrounding vortices, indicating that the riblets in the near-wall area play a rectifying and slowing effect on the vortex motion. However, for the smooth-plate case, the near-wall area is filled with twisted and disordered vortices with different sizes. The velocity of the near-wall vortices is significantly larger in the case of the smooth-plate case than in the case of the riblets case, which shows a slow near-wall turbulent flow.

4 Conclusions

To explore the turbulence properties associated with drag reduction, large-scale solving of the spatial developing turbulent boundary layers in a smooth flat plate and a riblet-mounted flat plate has been implemented by a high-order precision finite difference solver. Long enough distance for the flat plate ensures that the turbulent Reynolds number is up to 500. The 2D triangular riblets with $s^+ \approx 30.82$, $h^+ \approx 15.41$ are installed in the downstream section of the smooth flat plate where the Re_θ exactly ranges from 2107 to 2332. The purpose is to observe the effects of riblets control on the friction drag at the largest possible Reynolds number. By comparing the changes

in turbulence structure and drag characteristics in these two cases, the primary conclusions could be drawn as follows.

(1) A global drag reduction rate of 1.276% is obtained in current riblet geometry and turbulent conditions, demonstrating the effectiveness of 2D triangular riblets control for skin-friction drag reduction. However, drag reduction is not available at any position of the riblet. In most locations inside the riblet, their average velocity profiles have upward shifts compared to the curve of the smooth flat-plate, indicating a relatively small wall friction velocity and a thickened viscous sublayer by riblets control. However, it is also noted that there is a slight downward shift of the log-law curve at the riblet tip, which causes an increase in the friction drag coefficient. In addition, the momentum Reynolds number and shape factor increase in the spatial development of the boundary layer by riblets control.

(2) The riblets control weakens the turbulent Reynolds normal stresses (u_{rms}, v_{rms}, w_{rms}) in three directions and their peak points are shifted outward. Moreover, due to the spanwise-mounted riblet array, the distributions of (u_{rms}, v_{rms}, w_{rms}) are regularly and periodically in the spanwise direction instead of being disordered like the smooth flat plate case. By quadrant analysis of Reynolds shear stress $-u'v'$, a reduction of turbulent ejection and sweep events is also observed, but the first and third quadrant events have no significant change, which commonly leads to a reduction of turbulent kinetic energy production with riblets control.

(3) The riblets play roles of lifting and rectification in terms of drag control. The streamwise vortices and their fluctuation structures are shifted upward by riblets, thus the interactions between them and the wall surface are weakened, which causes a decrease of both turbulent vorticity fluctuation and velocity fluctuation. In the inner of the boundary layer, the streaks of instantaneous streamwise velocity, streamwise fluctuation velocity and 3D vortices evolve from the distorted to long and straight structures as they pass through the riblets. This indicates that riblets turn turbulence into a more ordered state and cause the near-wall streaks to flow downstream at a lower velocity.

Declarations

References

1. Walsh MJ, Lindemann AM (1984) Optimization and application of riblets for turbulent drag reduction. Paper presented at the 22nd aerospace sciences meeting, AIAA 1984-347, Reno, 9-12 January 1984
2. Walsh MJ (1990) Effect of detailed surface geometry on riblet drag reduction performance. J Aircr 27(6):572–573
3. Luchini P, Manzo F, Pozzi A (1991) Resistance of a grooved surface to parallel flow and cross-flow. J Fluid Mech 228:87–109
4. Bechert DW, Bruse M, Hage W, Van der Hoeven JGT, Hoppe G (1997) Experiments on drag-reducing surfaces and their optimization with an adjustable geometry. J Fluid Mech 338:59–87
5. García-Mayoral R, Jiménez J (2011) Drag reduction by riblets. Phil Trans R Soc A 369(1940):1412–1427
6. García-Mayoral R, Jiménez J (2011) Hydrodynamic stability and breakdown of the viscous regime over riblets. J Fluid Mech 678:317–347
7. García-Mayoral R, Jiménez J (2012) Scaling of turbulent structures in riblet channels up to $Re_\tau \approx 550$. Phys Fluids 24(10):105101
8. Sasamori M, Mamori H, Iwamoto K, Murata A (2014) Experimental study on drag-reduction effect due to sinusoidal riblets in turbulent channel flow. Exp Fluids 55:1828
9. Bechert DW, Bartenwerfer M (1989) The viscous flow on surfaces with longitudinal ribs. J Fluid Mech 206:105–129
10. Bechert DW, Bruse M, Hage W (2000) Experiments with three-dimensional riblets as an idealized model of shark skin. Exp Fluids 28(5):403–412
11. Lee SJ, Lee SH (2001) Flow field analysis of a turbulent boundary layer over a riblet surface. Exp Fluids 30(2):153–166
12. Goldstein DB, Tuan TC (1998) Secondary flow induced by riblets. J Fluid Mech 363:115–151
13. Martin S, Bhushan B (2014) Fluid flow analysis of a shark-inspired microstructure. J Fluid Mech 756:5–29
14. Martin S, Bhushan B (2016) Modeling and optimization of shark-inspired riblet geometries for low drag applications. J Colloid Interf Sci 474:206–215
15. Bhushan B (2009) Biomimetics: lessons from nature–an overview. Phil Trans R Soc A 367(1893):1445–1486
16. Dean B, Bhushan B (2010) Shark-skin surfaces for fluid-drag reduction in turbulent flow: a review. Phil Trans R Soc A 368(1929):4775–4806
17. El-Samni OA, Chun HH, Yoon HS (2007) Drag reduction of turbulent flow over thin rectangular riblets. Int J Eng Sci 45(2–8):436–454
18. Choi H, Moin P, Kim J (1993) Direct numerical simulation of turbulent flow over riblets. J Fluid Mech 255:503–539
19. Chu DC, Karniadakis GE (1993) A direct numerical simulation of laminar and turbulent flow over riblet-mounted surfaces. J Fluid Mech 250:1–42
20. Boomsma A, Sotiropoulos F (2016) Direct numerical simulation of sharkskin denticles in turbulent channel flow. Phys Fluids 28(3):035106
21. Wen L, Weaver JC, Lauder GV (2014) Biomimetic shark skin: design, fabrication and hydrodynamic function. J Exp Biol 217(10):1656–1666
22. Szodruch J (1991) Viscous drag reduction on transport aircraft. Paper presented at the 29th aerospace sciences meeting, AIAA 1991-685, Reno, 7-10 January 1991
23. Viswanath PR (2002) Aircraft viscous drag reduction using riblets. Prog Aerosp Sci 38(6–7):571–600
24. Lee SJ, Jang YG (2005) Control of flow around a NACA 0012 airfoil with a micro-riblet film. J Fluids Struct 20(5):659–672
25. Rohr JJ, Andersen GW, Reidy LW, Hendricks EW (1992) A comparison of the drag-reducing benefits of riblets in internal and external flows. Exp Fluids 13(6):361–368
26. Klumpp S, Meinke M, Schröder W (2010) Numerical simulation of riblet controlled spatial transition in a zero-pressure-gradient boundary layer. Flow Turbul Combust 85(1):57–71
27. Boomsma A, Sotiropoulos F (2015) Riblet drag reduction in mild adverse pressure gradients: a numerical investigation. Int J Heat Fluid Flow 56:251–260
28. Zhang Y, Chen H, Fu S, Dong W (2018) Numerical study of an airfoil with riblets installed based on large eddy simulation. Aerosp Sci Technol 78:661–670
29. Zhang Y, Yan C, Chen H, Yin Y (2020) Study of riblet drag reduction for an infinite span wing with different sweep angles. Chin J Aeronaut 33(12):3125–3137
30. Nugroho B, Hutchins N, Monty JP (2013) Large-scale spanwise periodicity in a turbulent boundary layer induced by highly ordered and directional surface roughness. Int J Heat Fluid Flow 41:90–102
31. Kametani Y, Fukagata K, Örlü R, Schlatter P (2015) Effect of uniform blowing/suction in a turbulent boundary layer at moderate Reynolds number. Int J Heat Fluid Flow 55:132–142
32. Xie L, Zheng Y, Zhang Y, Ye ZX, Zou JF (2021) Effects of localized micro-blowing on a spatially developing flat turbulent boundary layer. Flow Turbul Combust 107(1):51–79
33. Schlatter P, Örlü R, Li Q, Brethouwer G, Fransson JHM, Johansson AV, Alfredsson PH, Henningson DS (2009) Turbulent boundary layers up to $Re_\theta = 2500$ studied through simulation and experiment. Phys Fluids 21(5):051702
34. Li XL, Fu DX, Ma YW, Liang X (2010) Direct numerical simulation of compressible turbulent flows. Acta Mech Sin 26(6):795–806
35. Zhou Y, Li XL, Fu DX, Ma YW (2007) Coherent structures in transition of a flat-plate boundary layer at $Ma = 0.7$. Chinese Phys Lett 24(1):147
36. Steger JL, Warming RF (1981) Flux vector splitting of the inviscid gasdynamic equations with application to finite-difference methods. J Comput Phys 40(2):263–293
37. Fan YT, Zhang Y, Ye ZX, Zou JF, Zheng Y (2020) Micro-blowing: Effect on flow characteristics in turbulent flat plate boundary layer and drag reduction mechanism. Acta Aeronaut Astronaut Sin 41(10):123814.
38. Lee JH, Sung HJ (2011) Direct numerical simulation of a turbulent boundary layer up to $Re_\theta = 2500$. Int J Heat Fluid Flow 32(1):1–10
39. Smits AJ, Matheson N, Joubert PN (1983) Low-Reynolds-number turbulent boundary layers in zero and favorable pressure gradients. J Ship Res 27(03):147–157
40. Spalart PR (1988) Direct simulation of a turbulent boundary layer up to $R_\theta = 1410$. J Fluid Mech 187:61–98

Zhang *et al. Advances in Aerodynamics*   *(2022) 4:29*

Page 28 of 28

41. Vukoslavcevic P, Wallace JM, Balint JL (1992) Viscous drag reduction using streamwise-aligned riblets. AIAA J 30(4):1119–1122
42. Metzger MM, Klewicki JC (2001) A comparative study of near-wall turbulence in high and low Reynolds number boundary layers. Phys Fluids 13(3):692–701
43. Park SR, Wallace JM (1994) Flow alteration and drag reduction by riblets in a turbulent boundary layer. AIAA J 32(1):31–38
44. Wang JJ, Lan SL, Chen G (2000) Experimental study on the turbulent boundary layer flow over riblets surface. Fluid Dyn Res 27(4):217

Publisher's Note

Springer Nature remains neutral with regard to jurisdictional claims in published maps and institutional affiliations.